APPENDIX

for Herbert et al.

"Chromatin stiffening underlies enhanced locus mobility after DNA damage in budding yeast"

Content:

Appendix Supplementary Methods

Effect of localization errors and locus mobility on measured intrachromosomal distances

Our measurements of distances between two loci are potentially affected by two types of errors: (i) localization errors and (ii) motion errors.

First, the (*x,y*) coordinates computed for each locus are affected by random errors because of the finite signal to noise ratio of the fluorescent spots (Ober *et al*, 2004). To estimate these errors we imaged a single locus labeled both in red and green (Thérizols *et al*, 2010) (see Materials and Methods) and compared the coordinates computed from each color channel. **Appendix Fig. S4a** shows the differences in *x*- and *y*-coordinates computed from the red and green images $dx = x_{\mathrm{G}} - x_{\mathrm{R}}$ and $dy = y_{\mathrm{G}} - y_{\mathrm{R}}$ for n=344 cells. The averages $\langle dx \rangle \approx 7$ nm and $\langle dy \rangle \approx 1$ nm (red cross) reflect residual systematic shifts due to uncorrected chromatic aberrations, and the standard deviations $\sigma(dx) \approx 32$ nm and $\sigma(dy) \approx 27$ nm reflect random localization errors.

Second, distances between loci are measured on 2D maximum intensity projections of a series of z-planes separated by Δz=300 nm that alternate green and red color images (**Appendix Fig. S4b**). Because the green and red spots usually have different z-coordinates ($z_{\mathrm{G}} \neq z_{\mathrm{R}}$), they are imaged at distinct times, t and $t' = t + \Delta t$, where $\Delta t = |z_{\mathrm{G}} - z_{\mathrm{R}}|/\Delta z \times 2\delta t$, where $\delta t = 100$ ms is the exposure time of each image. The mobility of the loci during the interval Δt therefore contributes to modifying the measured 2D distance d_{meas} from the true distance d_{true}.

In order to estimate the effect of these errors on measured distances, we simulated distance distributions with and without errors (**Appendix Fig. S4c,d**). To do this, we randomly positioned a red and a green locus in 3D space, at coordinates $(x_{\mathrm{G}}, y_{\mathrm{G}}, z_{\mathrm{G}})$ and $(x_{\mathrm{R}}, y_{\mathrm{R}}, z_{\mathrm{R}})$, respectively, with the difference between coordinates, $dx = x_{\mathrm{G}} - x_{\mathrm{R}}$, $dy = y_{\mathrm{G}} - y_{\mathrm{R}}$, and $dz = z_{\mathrm{G}} - z_{\mathrm{R}}$ drawn from random normal distributions with mean zero and variance $\sigma_R^2 = R_0^2/2$. This crated an isotropic distribution of the loci relative to each other and ensured that the distribution of 2D distances, $d_{\mathrm{true}} = \sqrt{(x_{\mathrm{G}} - x_{\mathrm{R}})^2 + (y_{\mathrm{G}} - y_{\mathrm{R}})^2}$, obeys approximately the same distribution as in the experimental data when R_0^2 is set to an experimentally measured mean squared distance (see **Fig. 2b, Fig. EV2** and the following section). We used $R_0 = 300$ nm for **Appendix Fig. S4c** and $R_0 = 800$ nm for **Appendix Fig. S4d**. These values bracket the root mean squared distances $\langle R^2 \rangle$ measured in our experiments. In order to simulate the effect of random localization errors, we simply added normally distributed random perturbations with mean zero and standard deviation $\sigma_{\mathrm{loc}} = 30$ nm to the coordinates x_{R} and y_{R} (yielding new coordinates x_{R}' and y_{R}'). In order to simulate the effect of motion, we added a another normally distributed perturbation to each coordinate, also with zero mean, but with a variance $\sigma^2_{\mathrm{motion}} = \frac{1}{2}\mathrm{MSD}(\Delta t)$, where MSD is the mean

squared displacement of the locus that was imaged last and the time interval Δt depends on the difference in axial coordinates, dz, as defined above. We used $\mathrm{MSD}(\Delta t) = 0.0388\,(\Delta t/2\ s)^{0.76}$ μm^2, based on the largest experimentally measured mean square displacements (locus Gr2 with 6 h Zeocin exposure, see **Fig. 1d**), thus providing an upper bound to the locus displacement.

We simulated thousands of pairs of loci as described and calculated three distance distributions : (i) the distribution of true distances, (ii) the distribution of distances with localization errors, and (iii) the distribution of distances with errors due to motion. The CDFs of these distributions are shown in **Appendix Fig. S4c,d** as solid blue curves, dashed orange curves, and red dotted curves, respectively. It is clear from this figure, that localization errors have a negligible effect on the distance distributions, and that the effect of motion is very minor. The localization errors modify the RMS distance by ~1% or less and the errors due to chromatin mobility by ~5% or less.

Ideal chain model

The simplest model of a polymer is an ideal chain model, in which interactions between monomers are ignored except between immediately consecutive monomers (Rubinstein & Colby, 2003). An ideal chain can be represented as a random walk of *N* steps of length *K*, where the orientation of each step relative to the previous one is uniformly random and independent of all preceding steps. The mean square distance between two monomers separated by *N* steps is: $\langle R^2 \rangle = NK^2 = LK$, where $L = NK$ is the linear length along the chain and $\langle . \rangle$ denotes an average over many chain configurations. The segment length *K* is twice the persistence length *P*: $K = 2P$. Expressed as function of the genomic distance *s* and the compaction *C*, the linear length is $L = s/C$ and the mean square distance is proportional to *s* with a slope of *P/C*: $\langle R^2 \rangle = 2Ps/C$. For large *N*, the probability density of the 2D vector $\boldsymbol{R}$ joining two monomers is a Gaussian: $p(\boldsymbol{R}) = \frac{1}{\pi R_0^2} \exp\left(-\frac{R^2}{R_0^2}\right)$ with $R_0^2 = \langle R^2 \rangle$. The probability density for the scalar distance *R* is then: $p(R) = 2\frac{R}{R_0^2} \exp\left(-\frac{R^2}{R_0^2}\right)$. The corresponding cumulative probability (i.e. the probability that for any given chain configuration the distance between the two monomers is smaller than or equal to *R)* is: $F(R; R_0) = 1 - \exp\left(-\frac{R^2}{R_0^2}\right)$.

Numerical chromosome simulations

For model predictions in **Fig. 5**, we used a Langevin dynamics simulation of chromosome IV in the yeast nucleus implemented using the LAMMPS engine (lammps.sandia.gov). A detailed description of the simulation is provided elsewhere (Arbona *et al*, 2017). Briefly, the chromosome was modeled as a chain of $W = 30$ nm

diameter beads connected to each other by FENE (finitely extensible non-linear elastic) potentials. The number of beads depended on the compaction *C*. Our reference model (black traces in **Fig. 5**) assumed a compaction of C = 50 bp/nm. The compaction was changed to 25 bp/nm and 110 bp/nm for the decondensed and condensed models, respectively, and the number of beads adjusted accordingly. No other changes to the simulation parameters were made; in particular the size W of the beads was not changed. An additional potential penalized large angles formed by three consecutive beads, ensuring a bending rigidity corresponding to a persistence length of P =27, 69 or 180 nm. Interactions between non-consecutive beads were modeled using truncated Lennard-Jones potentials. Additional potentials were introduced to model the tethering of centromeres to the spindle pole body (SPB) via microtubules, with an equilibrium length of L=300 or 500 nm, and the unspecific tethering of telomeres to the nuclear envelope, which was modeled as a confining sphere of radius 1 μm. The initial chain configuration was generated randomly in a sphere of larger radius, which was then progressively decreased down to 1 μm, after which point the potential modeling tethering to the SPB via microtubule was turned on. Chain motion was modeled using Langevin dynamics, wherein beads are subjected to random motions at each time step (Doi & Edwards, 1988). We ran four replica of the simulation, with $6*10^9$ steps for each. In order to compare the model's predictions to the experimental distance data (which were measured on 2D projections from 3D images), we computed predicted distances after randomly discarding one of the three coordinates at every step of the simulation.

The predicted mean square displacements of loci in **Fig. 5** were computed from the simulation trajectories in the same way as for the experimental data shown e.g. in Fig. 1. Comparison to the experimental data required scaling the simulation time steps to physical time. We fitted the scaling parameter, such that the MSD predicted by the reference model roughly matched the experimentally measured MSD for one locus in untreated cells (**Fig. 1d**, blue trace). This was done only once, and same scaling was applied for all loci and all simulated models.

To generate the simulated PALM/STORM images of a LacO array shown in **Fig. EV5**, we created random polymer configurations using a 3D freely rotating chain model, which consists of connected segments with a fixed angle θ between consecutive segments but a uniformly random torsion angle φ (Rubinstein & Colby, 2003). The angle θ is related to the persistence length P and the segment length l by: $\theta^2 = 2\,l/P$.

Locus pair	Common name	Strain		Reference
	Green-Red pair strains			
1	R1+ 89	YHB74-1-a	Mat a, ura3Δ0, leu2Δ0, his3Δ1, ade2-661, can1::HPHMX,ydr003w::tetO-TEF-URA3, iyGL117::TetR-mRFP-NATMX, , his3::HIS3-LacI-GFP, ydr042c::256lacO-TEF-LEU2	This study
2	R1+ 129	YHB75-1-alpha	Mat alpha, ura3Δ0, leu2Δ0, his3Δ1, lys2Δ202, ade2-661, can1::HPHMX, iyGL117::TetR-mRFP-NATMX, ydr003w::tetO-TEF-URA3, his3::HIS3-LacI-GFP, ydr068w::256lacO-TEF-LEU2	This study
3	R1+ 181	YHB76-4-a	Mat a, ura3Δ0, leu2Δ0, his3Δ1, lys2Δ202, ade2-661, can1::HPHMX, iyGL117::TetR-mRFP- NATMX, ydr003w::tetO-TEF-URA, , his3::HIS3-LacI-GFP, ydr095c::256lacO-TEF-LEU2	This study
4	R1+ 230	YHB77-1-a	Mat a, ura3Δ0, leu2Δ0, his3Δ1, lys2Δ202, ade2-661, can1::HPHMX, iyGL117::TetR-mRFP- NATMX, ydr003w::tetO-TEF-URA3, , his3::HIS3-LacI-GFP, ydr117c::256lacO-TEF-LEU2	This study
5	R2+ 122	YHB101-2-a	Mat a, ura3Δ0, leu2Δ0, his3Δ1, lys2Δ202, ade2-661, can1::HPHMX, iyGL117::TetR-mRFP- NATMX, ydr199w::tetO-TEF-URA3, , his3::HIS3-LacI-GFP, ydr259c::256lacO-TEF-LEU2	This study
6	R2+ 163	YHB102-1-a	Mat a, ura3Δ0, leu2Δ0, his3Δ1, ade2-661, can1::HPHMX, iyGL117::TetR-mRFP- NATMX, ydr199w::tetO-TEF-URA3, , his3::HIS3-LacI-GFP, ydr278c::256lacO-TEF-LEU2	This study
7	R2+ 202	YHB103-1-a	Mat a, ura3Δ0, leu2Δ0, his3Δ1, lys2Δ202, ade2-661, can1::HPHMX, iyGL117::TetR-mRFP- NATMX, ydr199w::tetO-TEF-URA3, , his3::HIS3-LacI-GFP, ydr297w::256lacO-TEF-LEU2	This study
8	R3 - 40	YHB219-1-alpha	Mat alpha, ura3Δ0, leu2Δ0, his3Δ1, lys2Δ202, ade2-661, iyGL117::TetR-mRFP- NATMX, ydr354w::tetO-TEF-URA3, , his3::HIS3-LacI-GFP, ydr336w::256lacO-TEF-LEU2	This study
9	R3 - 90	YHB218-1-alpha	Mat alpha, ura3Δ0, leu2Δ0, his3Δ1, ade2-661, iyGL117::TetR-mRFP- NATMX, ydr354w::tetO-TEF-URA3, , his3::HIS3-LacI-GFP, ydr316w::256lacO-TEF-LEU2	This study
10	R3 - 128	YHB217-2-alpha	Mat alpha, ura3Δ0, leu2Δ0, his3Δ1, lys2Δ202, ade2-661, iyGL117::TetR-mRFP- NATMX, ydr354w::tetO-TEF-URA3, HIS3::his3-LacI-GFP, ydr297w::256lacO-TEF-LEU2	This study
11	R3 - 167	YHB216-2-alpha	Mat alpha, ura3Δ0, leu2Δ0, his3Δ1, ade2-661, iyGL117::TetR-mRFP- NATMX, ydr354w::tetO-TEF-URA3, HIS3::HIS3-LacI-GFP, ydr278c::256lacO-TEF-LEU2	This study
12	R3 - 209	YHB215-2-alpha	Mat alpha, ura3Δ0, leu2Δ0, his3Δ1, lys2Δ202, ade2-661, iyGL117::TetR-mRFP- NATMX, ydr354w::tetO-TEF-URA3, , his3::HIS3-LacI-GFP, ydr259C::256lacO-TEF-LEU2	This study
13	R4 - 40	YHB157-1-alpha	Mat alpha, ura3Δ0, leu2Δ0, his3Δ1, ade2-661, ydr539w::112tetO-TEF-URA3, iyGL117::TetR-mRFP- NATMX, , his3::HIS3-LacI-GFP, ydr514C::256lacO-TEF-LEU2	This study
14	R4 - 78	YHB156-1-a	Mat a, ura3Δ0, leu2Δ0, his3Δ1, ade2-661, ydr539w::112tetO-TEF-URA3, iyGL117::TetR-mRFP- NATMX, , his3::HIS3-LacI-GFP, ydr491C::256lacO-LEU2	This study
15	R4 - 115	YHB155-1-alpha	Mat alpha, ura3Δ0, leu2Δ0, his3Δ1, ade2-661, ydr539w::112tetO-TEF-URA3, iyGL117::TetR-mRFP- NATMX, , his3::HIS3-LacI-GFP, ydr467C::256lacO-LEU2	This study
16	R4 - 160	YHB154-1-alpha	Mat alpha, ura3Δ0, leu2Δ0, his3Δ1, ade2-661, yDR539w::112tetO-TEF-URA3, iyGL117::TetR-mRFP- NATMX, his3::HIS3-LacI-GFP, ydr445C::256lacO-TEF-LEU2	This study
	Control Green-Red strain			
	YPT237	YPT237-a	yfr057w::KANMX::112tetO-URA3 ; iyGL117::TetR-mRFP NATMX lys2Δ202::TetR-GFP-LYS2	(Thérizols *et al*, 2010)
	Subtelomere XIIIR			

	YEF798	YEF798-a	lacO::LEU2::ymr320w::KANMX::HOcs, YIR040c KANMX::ClaI PMW47(ADE3-LEU2), his3::LacI-GFP::HIS3	(Agmon *et al*, 2013)
	Cep3 mutant			
	YEF1020	YHB76-1-a, cep3S575A	Mat a, iyGL117::TetR-mRFP-NATMX, ydr003W::tetO- URA3 , his3::HIS3-LacI-GFP, ydr095C::lacO- LEU2, cep3::cep3S575A-KANMX	This study
	H2A mutants			
3	YEF1030	YHB76-1-a H2A S129A	Mat a, iyGL117::TetR-mRFP-NATMX ydr003W::tetO- URA3 , his3::HIS3-LacI-GFP, ydr095C::lacO- LEU2 hta1::HTA1-S129A-KANMX , hta2::HTA2-S129A-ADE2	This study
7	YEF1028	YHB103-1-a H2A S129A	Mat a , iyGL117::TetR-mRFP-NATMX ydr199W::tetO- URA3 , his3::HIS3-LacI-GFP, ydr297W::lacO- LEU2 hta1::HTA1-S129A-TRP1, hta2::HTA2-S129A-ADE2	This study
12	YEF1032	YHB215-3-a H2A S129A	Mat a, iyGL117::TetR-mRFP -NATMX ydr354W::tetO- URA3 , his3::HIS3-LacI-GFP ydr259C::lacO- LEU2 hta1::HTA1-S129A-KANMX, hta2::HTA2-S129A-ADE2	This study
	Sae2 mutant			
11	YFGF8	YHB216-2-alpha, YGL175C::KNMX	Mat alpha, iyGL117::TetR-mRFP-NATMX, ydr354W::tetO-TEF-URA3 , his3::HIS3-LacI-GFP, ydr278C::lacO-TEF-LEU2, ygl175C::KANMX	This study
	Blm10 mutant			
11	YFGF9	YHB216-2-alpha, YFL007W::KNMX	Mat alpha, iyGL117::TetR-mRFP-NATMX, ydr354W::tetO-TEF-URA3 , his3::HIS3-LacI-GFP, ydr278C::lacO-TEF-LEU2, yfl007W::KANMX	This study
	CEN-SPB strains			
	YEF671	CENIV, SPC42::GFP	CENIV-tetO, TetR-GFP, spc42::SPC42::GFP-TRP1	(He *et al*, 2000)
	YEF1019	YEF671, SPC42::mCherry-HIS3	CENIV-tetO, TetR-GFP, spc42::SPC42:: mCherry-HIS3	This study
	YEF1024	YEF1019, cep3S575A	CENIV-tetO, TetR-GFP, spc42::SPC42:: mCherry-HIS3 , cep3 ::cep3-S575A-KanMX	This study

Appendix Table S1: List of yeast strains. The first and leftmost column indicates the number or letter referring to each strain in the text. Column 2 indicates which loci were labeled in red and green. For example, "R1, R1+ 89" means that locus R1 (the pericentromeric locus indicated in **Fig. 1c**) was labeled in red, and that a second locus was labeled in green at a distance of 89 Kb from locus R1 (plus signs mean that the second locus is closer to the right telomere of chromosome IV, minus signs mean that the second locus is closer to the centromere). Column 3 indicates the name of the strain. Column 4 indicates the genotype.

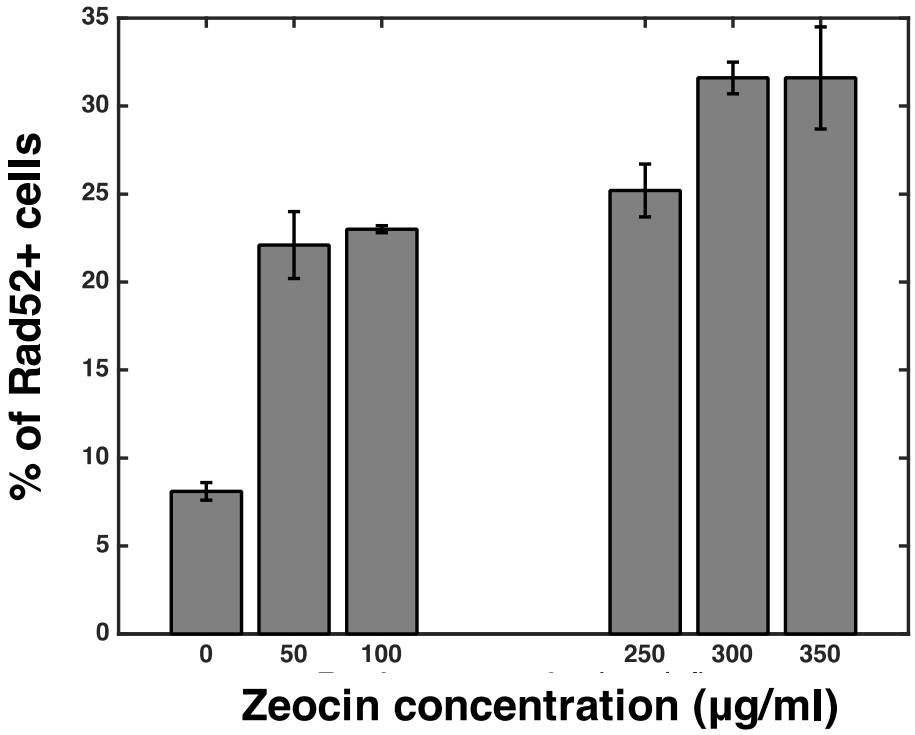

Appendix Figure S1: Effect of Zeocin concentration on DNA damage foci.

This bar plot shows the percentage of cells with at least one Rad52 focus as function of the concentration of Zeocin. Shown are averages from two independent experiments (3 independent experiments for the concentration 0), with error bars indicating standard deviation. The number of cells ranged from n=119 to 346 per experiment, with an average of 255.

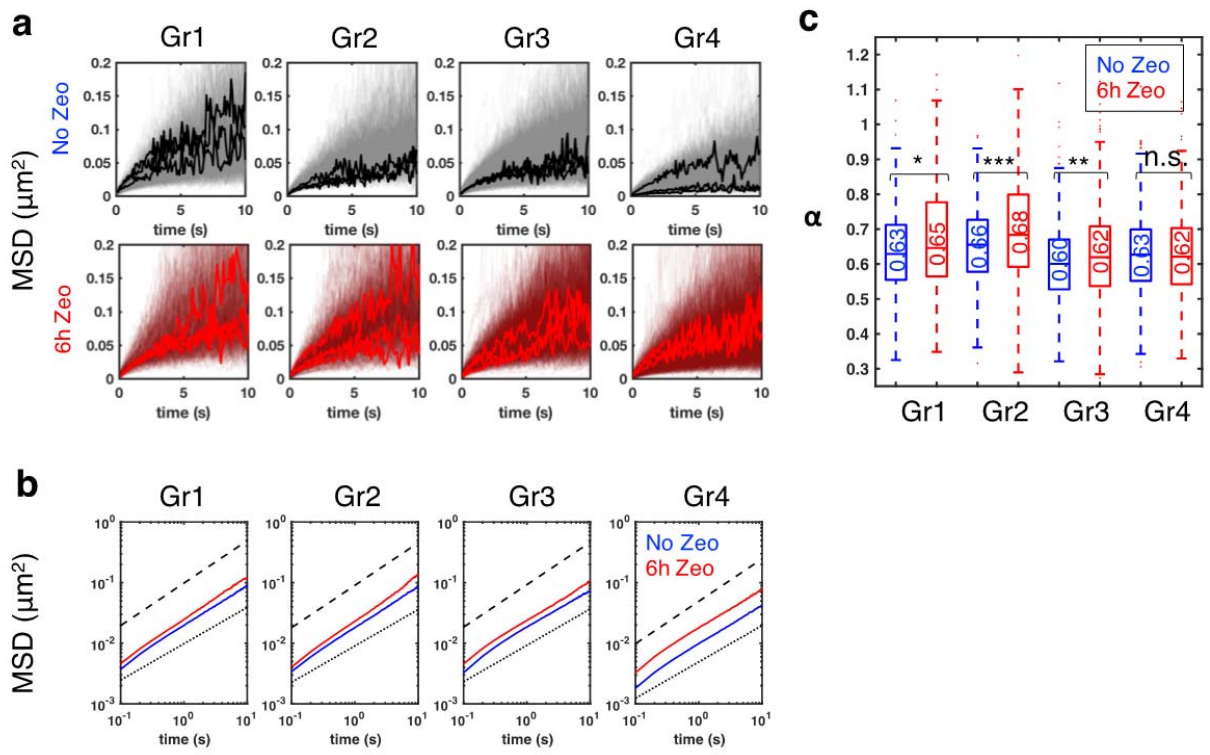

Appendix Figure S2: Mean square displacements (MSD) of chromatin loci with and without Zeocin treatment.

a) MSD of loci Gr1-Gr4 as function of time interval up to 10 seconds. Top row: without Zeocin, bottom row: after 6h of Zeocin treatment. MSD curves for all trajectories are shown in the background (semi-transparent grey or red lines). MSD curves for three randomly selected trajectories are shown superimposed as solid, non-transparent, black or red curves. **b)** Average MSD for loci Gr1-Gr4 as in Fig. 1d, but shown using logarithmic axes. Blue: without Zeocin, red: after 6h of Zeocin treatment. The dotted line indicates a power law with an exponent α = 0.6, the dashed line a power law with α = 0.7. **c)** Distribution of subdiffusion exponents α for loci Gr1-Gr4. A power law Dt^{α} was fitted for each individual trajectory. Boxplots show the distribution of fitted exponents α. The median value of α is indicated vertically. Brackets indicate the result of a ranksum test comparing two distributions of exponents α. Three stars (***) indicates p<0.001, two stars (**) indicates p<0.01, one star indicates p<0.05, 'n.s.' means not significant (p>0.05).

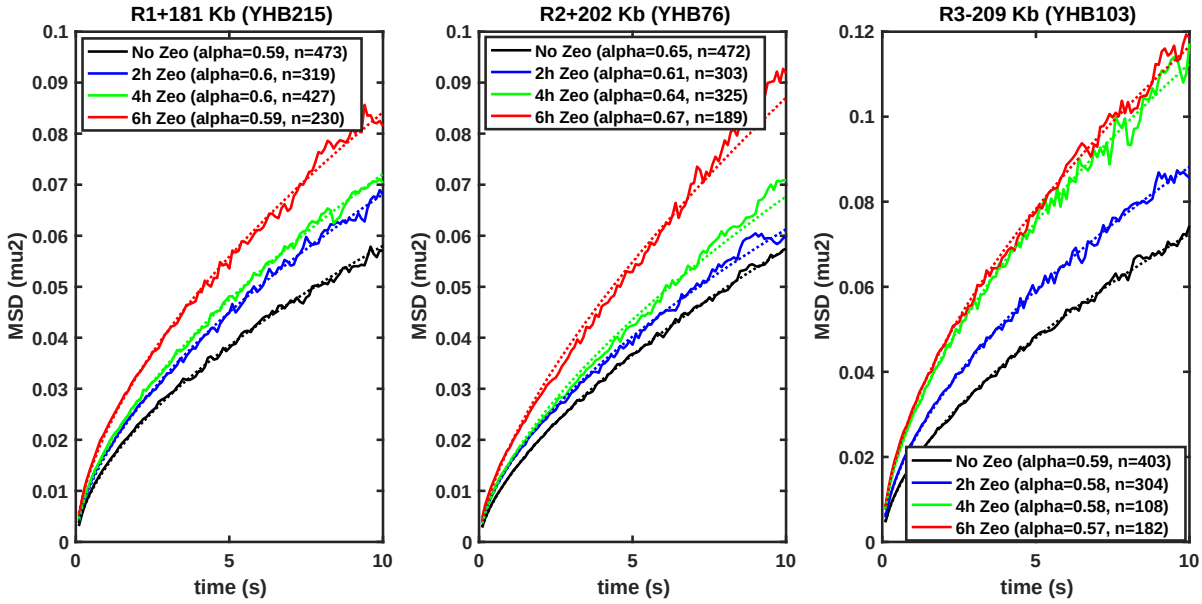

Appendix Figure S3: Longer Zeocin exposure leads to larger increase in chromatin dynamics.

This plot shows the average MSD of three loci on the right arm of chromosome IV. Solid curves are experimental data, dotted lines are fitted power laws Dt^{α}, with the exponent α as indicated in the legend. Color indicates the duration of Zeocin exposure. Black: no treatment, blue: 2h, green: 4h, red: 6h. The genomic location of the loci is indicated on top of each panel (see also Fig. 1c), and the yeast strain in parentheses. The number of cells analyzed for each MSD curve is indicated in the legend (n).

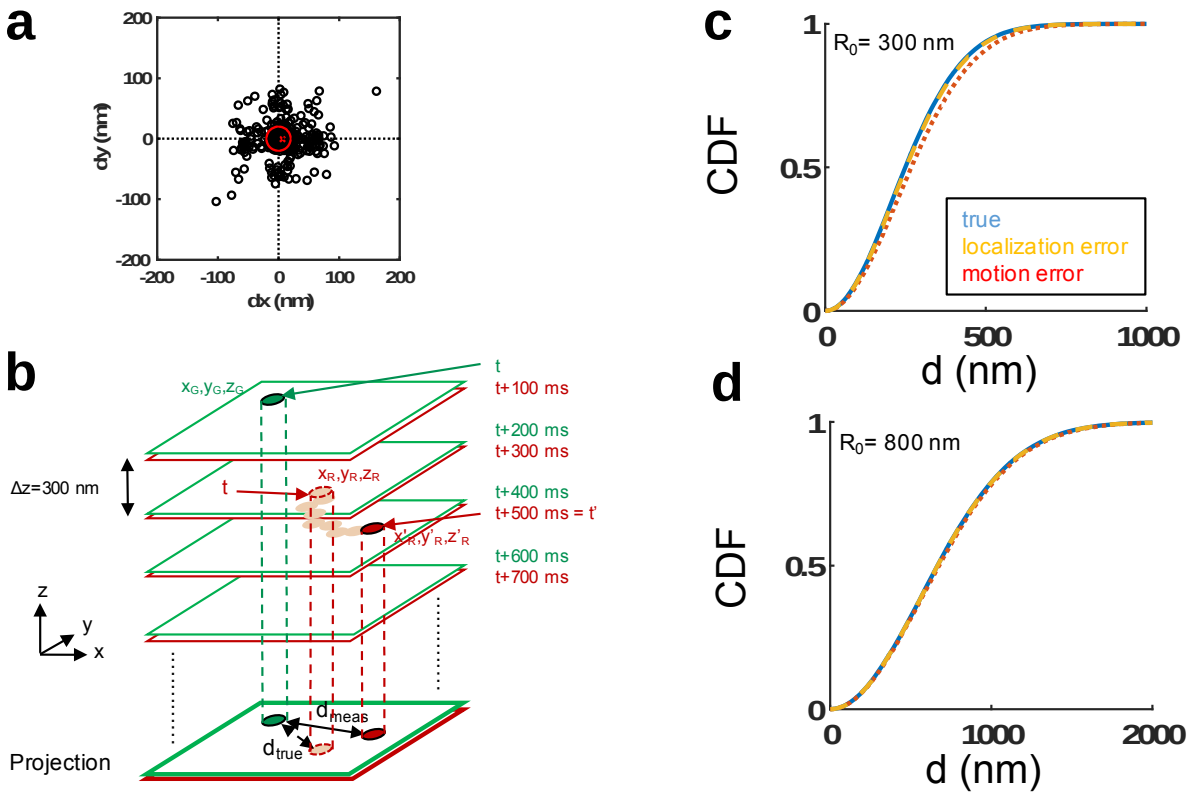

Appendix Figure S4: Effect of localization errors and motion on distance distributions.

This Figure accompanies section "Effect of localization errors and locus mobility on measured intrachromosomal distances" in the Appendix Supplementary Methods. (**a**) Scatter plot showing $dx = x_G - x_R$ and $dy = y_G - y_R$, the differences in x- and y-coordinates, computed from the red and green images of a Tet operator array labeled using both TetR-eGFP and TetR-mRFP in n=344 cells. The averages $\langle dx \rangle \approx 7$ nm and $\langle dy \rangle \approx 1$ nm (red cross) reflect residual systematic shifts due to uncorrected chromatic aberrations, and the standard deviations $\sigma(dx) \approx 32$ nm and $\sigma(dy) \approx 27$ nm are used to estimate random localization errors. (**b**) Distances between red and green loci are measured on 2D maximum intensity projections (bottom) of a series of z-planes (above) separated by Δz=300 nm. Images are taken alternatively in the green and red color channels, with an exposure time of $\delta t = 100$ ms. Because the green and red spots usually have different z-coordinates (here $z_G > z_R$), they are imaged at distinct times, t and $t' = t + \Delta t$, where $\Delta t = |z_G - z_R|/\Delta z \times 2\delta t$. If the second imaged locus has moved during Δt, its position at time t' (red oval with black outline) will differ from its position at time t (dashed red oval) and the actually measured distance d_{meas} differ from the true distance d_{true}. (**c,d**) Cumulative distribution functions (CDF) of simulated 2D distances between loci, for an assumed root mean squared distance R_0 (in absence of errors) of 300 nm (**c**) or 800 nm (**d**). Blue: without any measurement errors; dashed orange: with random localization errors $\sigma(dx) = \sigma(dy) = 30$ nm; dotted red: with errors due to motion, assuming mean squared displacements (MSD) obeying $\mathrm{MSD}(\Delta t) = 0.0388\,(\Delta t/2\ s)^{0.76}$ μm^2 .

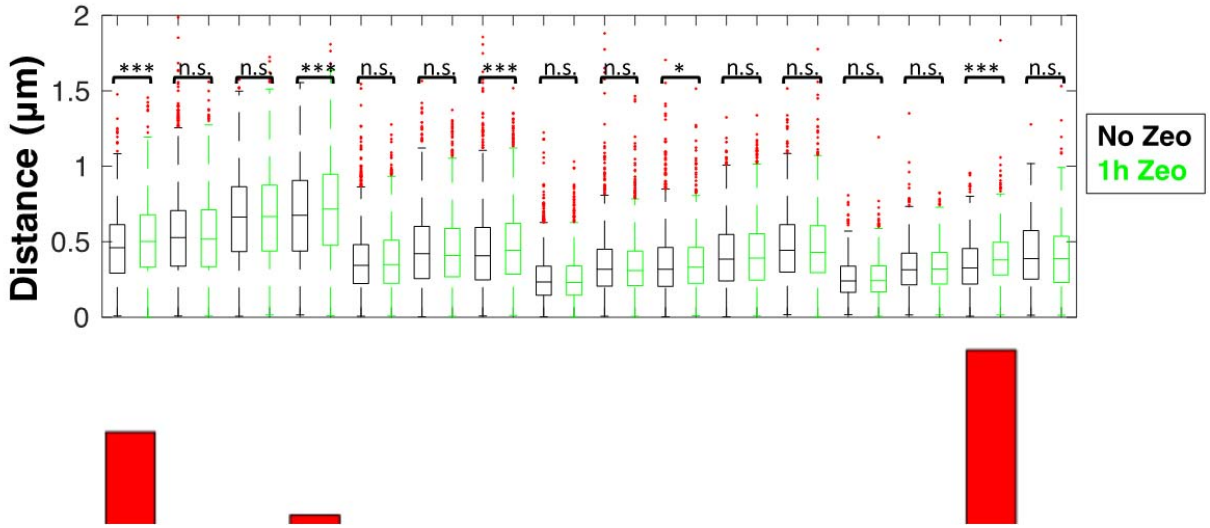

Appendix Figure S5: DNA damage after 1 hour of Zeocin treatment does not strongly alter intrachromosomal distances.

Boxplots show the distribution of intrachromosomal distances measured for 16 pairs of loci, in absence of Zeocin (black), and after 1 h of Zeocin treatment (green). Labels on the bottom indicate the pair of loci (see **Fig. 1c**). Brackets indicate the results of a Wilcoxon ranksum test on pairs of distributions, with 'n.s.' for not significant ($p>0.05$), * for $p<0.05$, ** for $p<0.01$ and *** for $p<0.001$.

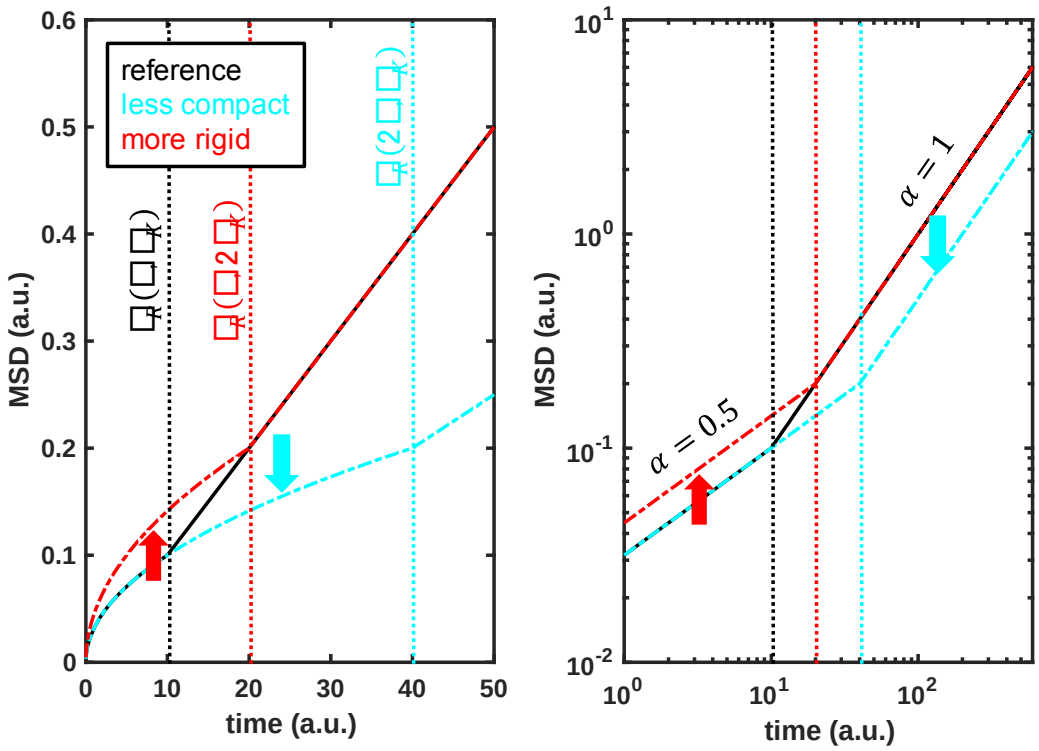

Appendix Figure S6: Rouse model predictions for chromatin dynamics upon decondensation or stiffening.

Mean squared displacement (MSD) as function of time for reference (black), decondensed chromatin (cyan) and stiffer chromatin (red) as predicted by a simple approximation of the Rouse polymer dynamics model (left: with linear scaling, right: with logarithmic scaling). For a polymer chain of total contour length (or curvilinear length) L and Kuhn length L_K (twice the persistence length, ie. $L_K = 2P$), this model predicts $MSD(t) \approx L_K(Dt)^{0.5}$ for $t \ll \tau_R$, and $MSD(t) \approx DL_K L^{-1} t$ for $t \gg \tau_R$, where D is the diffusion coefficient of a Kuhn segment, and $\tau_R(L, L_K) = L^2/D$ is the Rouse time; the Stokes-Einstein relation implies $D \propto L_K^{-1}$ (Rubinstein & Colby, 2003; Rosa & Zimmer, 2014). The black curve was obtained for $D = 0.1$, $L = 1$, and $L_K = 0.1$. The cyan curve corresponds to a decondensed (less compact) fiber, with the same Kuhn length but a doubled contour length ($L' = 2L, L'_K = L_K$). The red curve corresponds to a stiffer (more rigid) fiber, with double Kuhn length but the same contour length ($L' = L, L'_K = 2L_K$). Rouse times are indicated by dotted lines, and α is the exponent of the power law $MSD(t) \propto t^{\alpha}$. The reduction in chromatin mobility upon decondensation for $t > \tau_R(L, L_K)$ and the increase in chromatin mobility upon stiffening for $t < \tau_R(L, 2L_K)$ are apparent (arrows). Note that in the exact Rouse model, the cross-over between subdiffusion and diffusion is smooth, with α gradually increasing from 0.5 to 1 for $t < \tau_R$ and $t > \tau_R$, implying that decondensation can also reduce mobility at time scales below and above τ_R (as suggested by the shaded grey region). Complicating factors ignored by the Rouse model including nuclear confinement, tethering, and steric repulsion among monomers, are accounted for in the simulation results of **Fig. 5**.

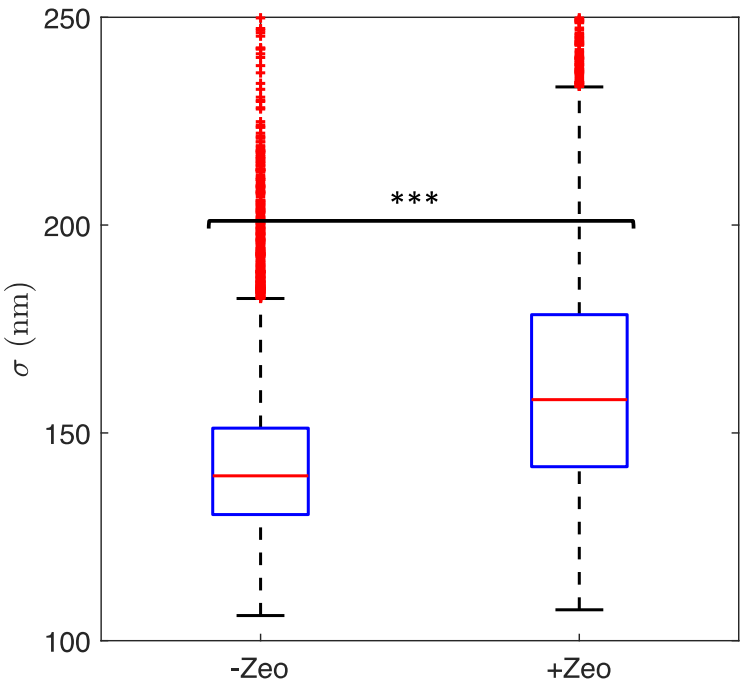

Appendix Figure S7: Increase in LacI-GFP spot size upon Zeocin treatment
Boxplots show the size distribution of LacI-GFP spots in untreated cells (-Zeo) and cells exposed to Zeocin for 6h (+Zeo). The value σ is the standard deviation of a Gaussian function fitted to each spot in maximum intensity projections of 3D widefield microscopy stacks. The increase in size upon Zeocin treatment is highly significant (Wilcoxon ranksum test $p<0.001$).

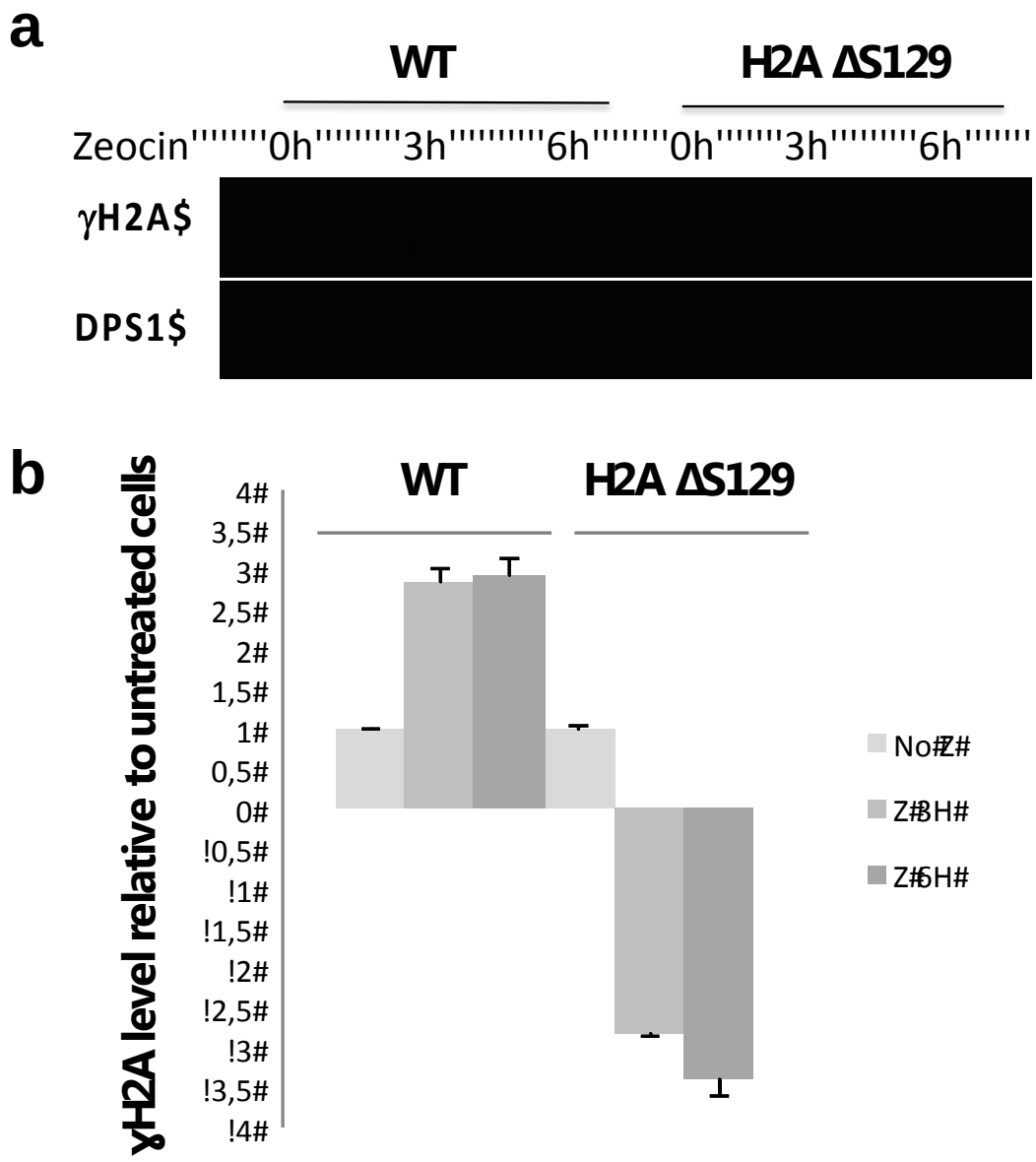

Appendix Figure S8: H2A increases upon Zeocin treatment in wild type cells, but not in a H2A S129A mutant.

a) Immunoblot using antibodies against H2A and the control protein PDS1 in wild type cells (WT) and mutants of H2A S129A, in which H2A is not phosphorylatable. **b**) Quantification of the level of γH2A upon exposure to Zeocin for 3h and 6h relative to untreated cells in wild type cells and the mutant.

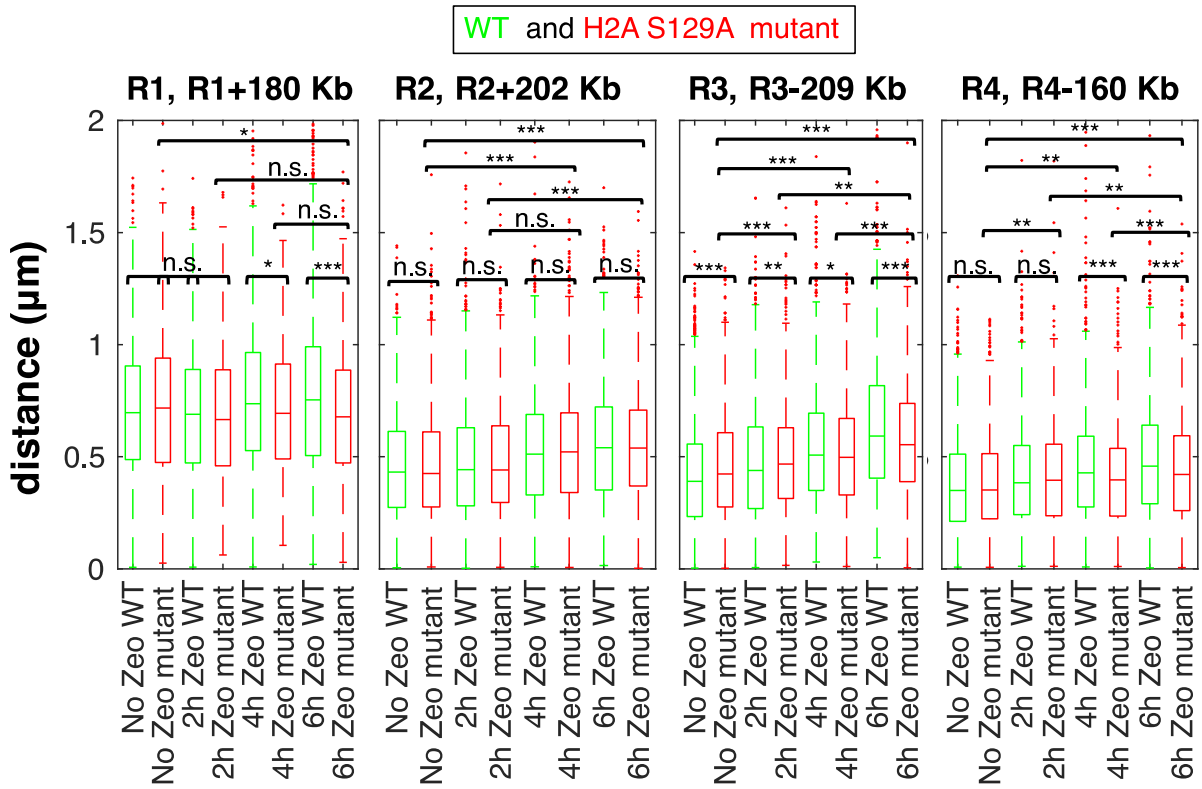

Appendix Figure S9: Effect of DNA damage on intrachromosomal distances in an H2A phosphorylation mutant compared to wild type cells.

Boxplots show the distribution of distances between four pairs of loci for increasing durations of Zeocin treatment. Green boxplots are from wild-type cells, red boxplots from to a mutant in which histone H2A cannot undergo phosphorylation. The pair of loci is indicated on the top of each panel. Labels on the bottom indicate the duration of Zeocin treatment (or its absence). Brackets indicate the results of a Wilcoxon ranksum test on pairs of distributions, with 'n.s' for non significant ($p>0.05$), * for $p<0.05$, ** for $p<0.01$ and *** for $p<0.001$.

Appendix Supplementary references:

Agmon N, Liefshitz B, Zimmer C, Fabre E & Kupiec M (2013) Effect of nuclear architecture on the efficiency of double-strand break repair. *Nat. Cell Biol.* **15:** 694–699

Arbona J-M, Herbert S, Fabre E & Zimmer C (2017) Inferring the physical properties of yeast chromatin through Bayesian analysis of whole nucleus simulations. *Genome Biol.* **18:** 81

Doi M & Edwards AM (1988) The Theory of Polymer Dynamics. Oxford University Press

He X, Asthana S & Sorger PK (2000) Transient sister chromatid separation and elastic deformation of chromosomes during mitosis in budding yeast. *Cell* **101:** 763–775

Ober RJ, Ram S & Ward ES (2004) Localization Accuracy in Single-Molecule Microscopy. *Biophys. J.* **86:** 1185–1200

Rosa A & Zimmer C (2014) Computational Models of Large-Scale Genome Architecture. In *International Review of Cell and Molecular Biology* pp 275–349.

Rubinstein M & Colby R (2003) Polymer physics Oxford University Press

Thérizols P, Duong T, Dujon B, Zimmer C & Fabre E (2010) Chromosome arm length and nuclear constraints determine the dynamic relationship of yeast subtelomeres. *Proc. Natl. Acad. Sci.* **107:** 2025